Journal of Alloys and Compounds 857 (2021) 157600

Contents lists available at ScienceDirect

Journal of Alloys and Compounds

journal homepage: http://www.elsevier.com/locate/jalcom

Significant roles of minor Mg addition in microstructural evolution and mechanical properties of cast Al—3Li—2Cu-0.15Zr alloy

Liang Wu [a, b], Xianfeng Li [a, *], Haowei Wang [a, b]

[a] State Key Laboratory of Metal Matrix Composites, Shanghai Jiao Tong University, No. 800 Dongchuan Road, Shanghai, 200240, PR China
[b] School of Materials Science and Engineering, Shanghai Jiao Tong University, No. 800 Dongchuan Road, Shanghai, 200240, PR China

ARTICLE INFO

Article history:
Received 24 August 2020
Received in revised form
11 October 2020
Accepted 13 October 2020
Available online 14 October 2020

Keywords:
Cast Al—Li—Cu alloys
High Li content
Microalloying
Microstructural evolution
Mechanical properties

ABSTRACT

The impact of minor Mg addition on microstructure and mechanical properties of cast Al—Li—Cu—Zr alloy with high lithium content (3 wt % Li) were studied to understand a qualitative assessment of sequence and kinetics of multiple precipitations and its effect on mechanical properties. Scanning Electron Microscope and X-ray diffraction results suggested that raising the content of Mg gradually altered the grain structure of the as-cast alloys and increased the types and volume fraction of the grain boundary intermetallic phase. Unusually, solvus temperature is higher than solidus temperature in 0.5 Mg alloy (Al—3Li—2Cu-0.5Mg-0.15Zr, wt. %), resulting in the incipient melting of the matrix before the complete dissolution of the intermetallic phases. Prominent enhancements in both age-hardening and precipitation kinetics of the base alloy with the addition of Mg were also easily identified, indicating the important role of Mg during isothermal aging. Transmission Electron Microscope and atom probe tomography results showed that minor Mg addition (0.2 wt %, denoted by 0.2 Mg alloy) could encourage the diffusion of Cu atoms by the aggregation of Mg—Cu-vacancy co-clusters, thereby promoting the nucleation of the T_1-Al_2CuLi and θ′-Al_2Cu precipitates. In addition, S′-Al_2CuMg precipitate was therefore introduced as a result of Mg addition. With further increasing the content of Mg to 0.5 wt %, the nucleation and growth of S′ precipitate would be promoted at the expense of T_1 and θ′ precipitates, especially the latter. Based on the theoretical models and regression analysis, the formation mechanism of δ′-Al_3Li precipitate-free-zones gradually changed from the initial vacancy-depletion mechanism to the solute-depletion mechanism, and Mg element could significantly inhibit the coarsening of δ′ precipitate-free-zones. The best balance between ductility and strength was obtained by 0.2 Mg alloy aged for 32 h, and the alloys have significant advantages in terms of density (2.437 g/cm^3) and elastic modulus (82.65 GPa) over conventional cast aluminum alloys (density: 2.7—2.8 g/cm^3; elastic modulus: 72 GPa).

1. Introduction

Age-hardening alloys based on the Al—Li system are of great interest for advanced structural components owing to their excellent combination of high elastic modulus, lightweight, and high strength [1—3]. Li element offers the substantial reduction in density and dramatic increase in stiffness compared with traditional Al alloys [4,5]. Nowadays, considerable number of reports on thermomechanical processing regimes, precipitation sequence, and deformation mechanism of deformed Al—Li alloys are available [6—8]. Few literatures, however, are obtainable on the design of alloy chemistry, mechanical properties, and microstructure characteristics of cast Al—Li alloys, especially those with high-Li-content (>2 wt %). One main reason is the overall performance of deformed alloys is superior to that of cast Al—Li alloys. This work is devoted to the development of cast Al—Li alloys, due to that casting is not only a cost-effective approach to manufacture components of complex shapes, but also an effective method to alleviate the anisotropy of mechanical properties. Most importantly, cast Al—Li alloys are more effective in reducing weight and increasing stiffness, because the upper limit of Li content in cast Al—Li alloys could be much higher than that of deformed alloys.

In Al—Li binary alloys, $L1_2$-Al_3Li (δ′) precipitate is the most important strengthening precipitate determining the mechanical properties of the alloys [9]. The ordered δ′ precipitate is fully coherent with aluminum matrix [10] and was reported to be

* Corresponding author.
E-mail address: brucelee75cn@sjtu.edu.cn (X. Li).

https://doi.org/10.1016/j.jallcom.2020.157600
0925-8388/

relatively stable at 175 °C [11,12]. It is well known that δ′ precipitates increase the strength of alloys. The planar slip caused by the shear of δ′ precipitates, however, is recognized as the main reason for low toughness and ductility [13]. To achieve high strength while maintaining appropriate ductility, the content of Li was determined to be 3 wt % to balance the gains and losses of lithium addition [14,15]. From a microstructure point of view, an effective method to further enhance the properties of cast Al–Li alloys is to optimize alloying compositions, e.g., introducing additional alloying elements such as Cu element [16,17], which leads to the so-called Al–Li–Cu based alloys. The addition of Cu element would generate a complex precipitation sequence, including T_1-Al_2CuLi, T_2-Al_6CuLi_3, and θ′-Al_2Cu phases, during isothermal aging and increase the overall density of the alloys inevitably [18]. Hence, the content of Cu was determined to be 2 wt % to improve mechanical properties while maintaining a relatively low density. However, most T_1 and θ′ precipitates tend to nucleate heterogeneously on the defects [19] and the density of dislocations or other defects in cast alloys is low, which leads to a low volume fraction and uneven distribution of θ′ and T_1 precipitates. It was proposed [20–22] that by pre-deforming the alloys prior to aging, a large number of dislocations could be introduced to promote the precipitation of T_1 and θ′ precipitates. Unfortunately, pre-deformation is not suitable for casting Al–Li alloys with complex shapes. Alternatively, microalloying with suitable elements, which could significantly alter the sequence and kinetics of precipitation, is recognized as an effective method to enhance the comprehensive performance of cast Al–Li–Cu alloys [23].

Thus, our research aims to study the impact of magnesium on microstructural evolution and mechanical properties of cast Al–3Li–2Cu-0.15Zr alloy to develop a new high-stiffness and low-density cast Al–Li–Cu alloy with excellent comprehensive performance. The reasons for selecting Mg element as the research object are as follows: (1) Mg is one of the commonly used microalloying elements in aluminum alloys, and its density is slightly lower than aluminum, which will not cause the increase of the overall density; (2) Mg has been extensively studied in deformed Al–Li alloys and proved to be beneficial for enhancing the comprehensive performance [7]; (3) The addition of Mg may introduce new precipitate that cannot be cut by dislocations, which is expected to disperse the planar slip and improve the ductility [24]; (4) Mg can also play the role of solid solution strengthening in the matrix [23]; (5) There are few reports about the effects of Mg element in cast high-Li-content Al–Li–Cu alloy (Li content > 2 wt %), and the mechanism is not yet clear. The main purpose of adding Zr element is to reduce the grain size and introduce the metastable, coherent β′-Al_3Zr phase, and the specific roles of β′ phases have been detailed elsewhere [25].

2. Materials and methods

Three alloys were specifically produced by the conventional casting method and the details of the melting procedures are available in our previous report [9]. The actual compositions of three experimental alloys, as listed in Table 1, were determined using Inductively Coupled Plasma-Optical Emission Spectroscopy (ICP-OES) and they are hereafter denoted as 0 Mg, 0.2 Mg, and 0.5 Mg alloys, respectively. The standard Archimedes method was used to determine the density of the alloys, and the averaged results of three tests are also shown in Table 1. The proper solution parameters were determined by the differential scanning calorimetry (DSC, 204F1) apparatus. The as-cast specimens were heat treated by a two-step solution treatment listed in Table 1, followed by isothermal aging at 175 °C in an oil bath. Each step was terminated by water-quenching. Vickers hardness was determined on mechanically polished samples (to a 0.02 μm finish) by a CARAT 930 Automatic Vickers hardness testing machine with a load of 10 kg and a dwell time of 15 s. The results are averaged from five measurements. Metallographic samples were mechanically polished. The elastic modulus was determined by a dynamic method, which was carried out on an ET-RT modulus tester (JE2-C1, Nihon Techno-Plus, Japan) according to the GB/T 22,315-2008 standard [26]. An Ultima IV X-ray diffractometer (XRD) was applied to identify the phase constitutions of as-cast alloys. Scanning Electron Microscope (SEM, TESCAN MAIA3 model 2016) and Optical microscope (OM, Zeiss Imager A1m) were used to observe the microstructure. The polished specimens were subjected to the X-ray photoelectron spectroscopy (XPS, Ulvac-PHI 5000 VersaProbe III) tests to detect the distribution of elements on the surface. Tensile tests of sheet specimens were conducted on Zwick/Roell universal testing machine with a strain rate of 1×10^{-4} s^{-1}. Sheet tensile samples of 3.5 mm in width, 2.0 mm in thickness, and 18 mm in gauge length were cut from the casting ingots by the electric-sparking wire-cutting machine [27]. Every tensile value was determined as the average of three test results. Selected samples were examined by transmission electron microscopy (TEM, JEOL 2100 microscope). Thin foils of the alloy samples were obtained by mechanical polishing and final electro-polishing, using a mixed solution of 25% nitric acid and 75% methanol at −35 °C and 30 V. Specimens for local-electrode atomprobe tomography (APT) were prepared by electropolishing with a mixed solution of 25% perchloric acid and 75% glacial acetic acid at 25 V, followed by 2% perchloric acid in butoxyethanol at 14 V. APT analysis was carried out by a LEAP-5000XR microscope, which was operated in voltage pulsed mode with a pulse fraction of 20%, a pulse repetition rate of 200 kHz, and a specimen temperature of 30 K. The commercial software (Cameca IVAS 3.8.1) was used for data reconstruction and visualization.

3. Results and discussion

3.1. Phase analysis and as-cast microstructure

Fig. 1 displays the phase constitutions of as-cast Al–3Li–2Cu-xMg-0.15Zr alloys. In as-cast 0 Mg alloy, the microstructure primarily consisted of intermetallic phases, such as δ′-Al_3Li, T_1-Al_2CuLi, θ-Al_2Cu, T_2-Al_6CuLi_3, and δ-AlLi phases, and α-Al matrix, which is consistent with the previous investigation [15]. It is well known that the formation of θ-Al_2Cu, T_2-Al_6CuLi_3, and δ-AlLi phases is produced by the non-equilibrium solidification process. In the patterns of as-cast 0.2 Mg and 0.5 Mg alloys, the intensity of the peaks arisen from δ′, T_1, and T_2 phases was much higher than those in 0 Mg alloy, and the intensity increased with increasing Mg content. It has been reported that [28] Mg could be incorporated

Table 1
The actual compositions, density, elastic modulus, and solution parameters of Al–3Li–2Cu-xMg-0.15Zr alloys in this work (wt.%).

Alloys	Measured chemical composition					Density (g/cm^3)	Modulus (GPa)	Solution parameters
	Li	Cu	Mg	Zr	Al			
0 Mg	2.96	1.86	–	0.12	Bal.	2.437	82.64	500 °C × 32 h + 560 °C × 24 h
0.2 Mg	3.06	1.83	0.22	0.13	Bal.	2.437	82.65	500 °C × 32 h + 560 °C × 24 h
0.5 Mg	3.04	1.92	0.47	0.12	Bal.	2.435	82.77	500 °C × 32 h + 560 °C × 36 h

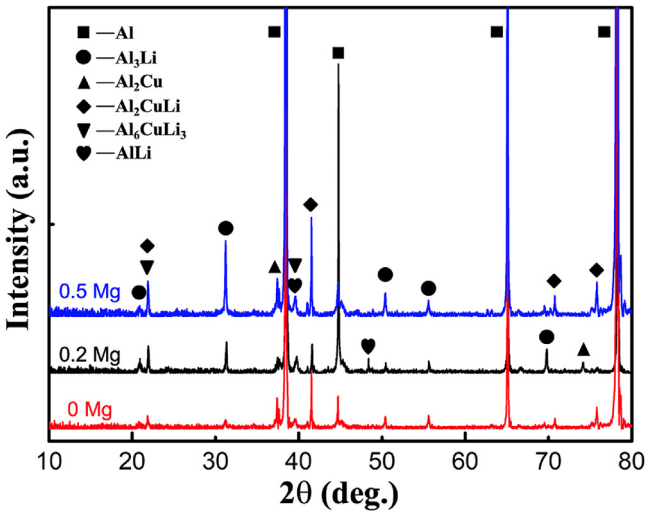

Fig. 1. XRD results of as-cast Al−3Li−2Cu-xMg-0.15Zr alloys.

into T_1 and T_2 phases in form of $Al_2(Cu, Mg)Li$ and $Al_6Cu(Li, Mg)_3$, respectively. These two phases are the main grain boundary intermetallic phases of the alloys with high ratio of Cu and Mg, which may because of the strong affinity between Cu and Mg atoms. Moreover, some authors [2,29] suggested that the addition of Mg could decrease the solubility of Li element in aluminum alloys, thereby promoting the formation of δ′ phase. However, according to the literatures [30,31], T_B-$Al_{7.5}Cu_4Li$ and S−Al_2MgLi phases also coexisted in quaternary Al−Li−Cu−Mg alloy. The absence of the diffraction peaks associated with these two phases in the patterns may be owing to their low contents.

The optical microstructures of as-cast Al−3Li−2Cu-xMg-0.15Zr (x = 0, 0.2, 0.5) alloys are shown in Fig. 2. The as-cast microstructures of the three alloys were similar, and the matrix consisted of coarse intermetallic phases in the inter-dendritic region or at the grain boundary and typical dendritic α-Al grains. The volume fraction of the grain boundary intermetallic phases increased with the increase of Mg content. Zhang and co-authors [32] reported that as the content of Mg increased from 0 to 2 wt%, the grain structure was refined gradually, and the microstructure of as-cast alloys transformed into a combination of dendritic and equiaxed grains, which is mainly owing to the enrichment of solute at the solid/liquid interface during solidification, i.e. constitutional undercooling [33]. The grain refinement effect of the Mg element in this work, however, is not significant, which may be due to the small amount of Mg added.

Fig. 3a displays the un-etched SEM micrograph of as-cast 0.5 Mg alloy, and the distributions of different solute elements acquired by EDS are shown in Fig. 3b−d. Note that similar results of 0 Mg and 0.2 Mg alloys are thus not given here anymore. The distribution of Cu element is highly coincident with that of intermetallic phases, which is distributed along the grain boundary [34]. However, these Cu-containing intermetallic phases, such as θ, T_2, and T_1, have not been identified since Li element cannot be detected by EDS. Furthermore, Mg also has a slight segregation tendency at the grain boundaries.

3.2. Solution parameters and as-quenched microstructure

Fig. 4 shows the high-temperature range (450−700 °C) of the DSC curves of the alloys. A distinct endothermic peak, which is located at 560 ± 2 °C in three alloys, is attributed to the dissolution of Cu-containing intermetallic phases according to the results of XRD test and previous report [9]. Furthermore, the amount of Cu-containing intermetallic phases increases along with the increase of Mg content, resulting in the higher difficulty to completely dissolve intermetallic phases. Note that, the position of the endothermic peak does not move significantly in the alloys with different Mg contents, but its integral increases obviously. This indicates that the amount of the Cu-containing intermetallic phases increases dramatically, which is also confirmed by the XRD results. Based on the existence of several Cu-containing intermetallic phases with different melting points in the as-cast alloys, a two-step solution treatment was selected to dissolve these Cu-containing intermetallic phases. The homogenization temperature commonly used in the cast Al−Cu alloys, 500 °C, was determined as the safe temperature of the first step [27], which, however, is insufficient to completely dissolve all the Cu-containing intermetallic phases according to the DSC results. Therefore, a relatively higher temperature for the second step (560 °C) was selected to further decrease the amount of these intermetallic phases and improve the supersaturated solid solubility of solute atoms without the occurrence of incipient melting.

The typical microstructures of as-quenched Al−3Li−2Cu-xMg-0.15Zr alloys are shown in Fig. 5. In as-quenched samples, the bulk of Cu-containing intermetallic phases in 0 Mg and 0.2 Mg alloys were completely dissolved, while some residual intermetallic phases were still observed at the triple junctions in 0.5 Mg alloy. This indicates that the second-step temperature, 560 °C, is also insufficient to completely dissolve all the Cu-containing intermetallic phases. The application of a higher temperature (570 °C), however, resulted in a typical incipient melting feature (illustrated in Fig. 6b). Even so, a large amount of residual intermetallic phases was still observed in the sample treated at 570 °C, as shown in Fig. 6a (marked by black arrows). Two empirical formulas were established for quaternary Al−Li−Cu−Mg alloys by Dorward et al. [35] to evaluate the solvus and solidus temperatures, which could be calculated from the content of solute elements by the following formula:

From the above equations, the theoretical and of the 0.5 Mg alloy are 572.5 °C and 568.1 °C, respectively. Generally, is the lowest temperature required for completely dissolving intermetallic phases, which should be lower than . However, the opposite result was obtained for the 0.5 Mg alloy. This is a good explanation for the reason why raising the solution temperature does not completely dissolve the intermetallic phases but causes the incipient melting.

Fig. 7 shows the typical solute elements distribution of residual intermetallic phases in as-quenched 0.5 Mg alloy, indicating that this is a (Li, Cu, Mg)-rich phase. The distribution of solute elements within this phase, however, is uneven. The central area of the residual intermetallic phase is the enrichment area of Al, Li, Cu, and Mg elements, while the outer area is mainly the enrichment area of Li and Cu. This residual intermetallic phase was failed to be identified due to the complex composition and uneven distribution of the elements. Undoubtedly, these residual phases will greatly damage the mechanical properties.

3.3. Mechanical properties and vickers hardness

Fig. 8a displays the Vickers hardness values of the alloys which varies versus time at 175 °C. The initial hardness values of 0.2 Mg and 0.5 Mg alloys were greater than that of 0 Mg alloy as a result of the promoted nucleation of δ′ precipitates in the as-quenched state [23]. In addition, Mg element also played the role of solid solution strengthening in the matrix. Moreover, a decrease in peak-aged time and an increase in peak-aged hardness were observed after adding Mg to the base alloy, as indicated by the green arrow. The kinetics and response of age-hardening in three alloys were similar,

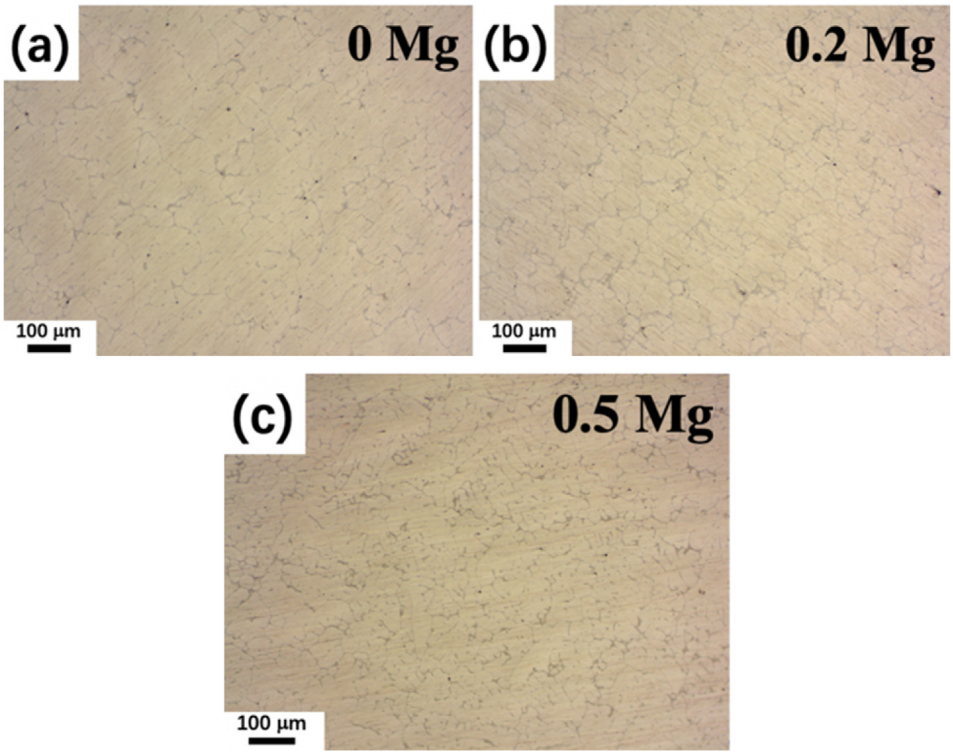

Fig. 2. The microstructures of as-cast Al−3Li−2Cu-xMg-0.15Zr alloys: (a) 0 wt%; (b) 0.2 wt%; (c) 0.5 wt%.

and the highest peak-hardness was obtained in 0.5 Mg alloy (178.1 HV), followed by 0.2 Mg and 0 Mg alloys. It is worth noting that the maximum incremental in hardness of the 0 Mg and 0.2 Mg alloys during isothermal aging (the difference between the hardness values of the peak-aged and the as-quenched) is about 80 HV, which is much larger than that of the 0.5 Mg alloy (only about 64 HV). This may be attributed to the large amount of residual intermetallic phases in 0.5 Mg alloy which consumes many solute atoms, leading to the weakening of the age-hardening effect.

Fig. 8b−d displays the tensile test results, including yield strength (YS), ultimate tensile strength (UTS) and elongation (EL), of the Al−3Li−2Cu-xMg-0.15Zr alloys in different aging states. As shown in

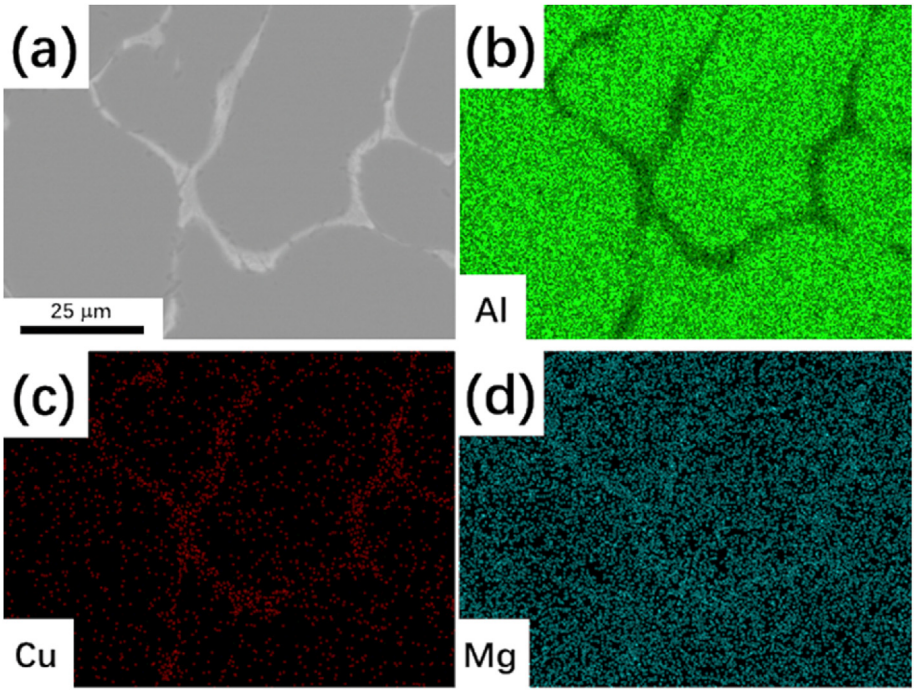

Fig. 3. (a) SEM micrograph of as-cast 0.5 Mg alloy; (b−d) the corresponding distribution of solute elements.

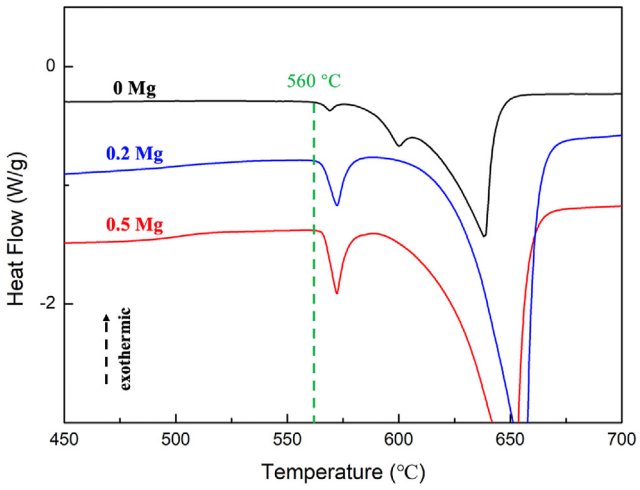

Fig. 4. DSC curves of the as-cast Al–3Li–2Cu-xMg-0.15Zr alloys.

Fig. 8b–d, YS of three alloys in all states increased almost linearly with the increase of Mg content. In contrast, UTS firstly increased and then decreased. The highest UTS, which is 415 MPa, was obtained by 0.2 Mg alloy aged at 175 °C for 32 h (Fig. 8d). As anticipated, EL decreased with extending aging time, which is contrary to the trends of YS and UTS. After aging, a small amount of Mg (0.2 wt %) was proven to significantly enhance YS and UTS of the alloy without much sacrifice of the ductility, as shown in Fig. 8c and d. Compared with 0 Mg and 0.2 Mg alloys, there is a significant decrease in EL of 0.5 Mg alloy. This sharp reduction of EL is mainly ascribed to the undesirable residual intermetallic phases in the as-quenched state. The best balance between strength (UTS = 415 MPa, YS = 337 MPa) and ductility (EL = 2.2%) was obtained by 0.2 Mg alloy aged at 175 °C for 32 h. The significant role of minor Mg addition in the kinetics and sequence of precipitation will be discussed in the following section.

It is worth mentioning that the density and elastic modulus of the alloys have great advantages over traditional cast aluminum alloys. The density of the alloys studied in this work, 2.437 g/cm^3, is significantly lower than those of the traditional aluminum alloys (2.7–2.8 g/cm^3), while the elastic modulus (82.65 GPa) is significantly greater than those of the conventional aluminum alloys (about 72 GPa).

3.4. Precipitation kinetics and sequence

In order to better explain the relationship between performance and microstructure, the samples of the alloys in various aging states, including 0 h (as-quenched, AQ), 32 h (under-aged, UA), x h (peak-aged, PA), and 600 h (over-aged, OA), were examined by TEM in detail. Note that unless otherwise specified, dark-field micrographs were obtained from superlattice reflections of δ′ phase.

Before aging, the heterogeneous dispersion of β′-Al_3Zr particles (formed during heat treatment) and the homogeneous distribution of fine δ′-Al_3Li precipitates were clearly observed in the matrix of 0 Mg alloy, as illustrated in Fig. 9. The $L1_2$ superlattice reflections from δ′ precipitates could also be clearly identified in the corresponding diffraction pattern, which is consistent with the previous report [36]. It has been suggested that precipitation behavior of Al–Li alloys in the initial stage of aging is mainly determined by Li content, and the homogeneous distribution of fine δ′ precipitates can always be observed in the as-quenched sample containing more than 2 wt % Li [37]. The congruent ordering prior to decomposition into δ′ precipitate and the solid solution could provide a plausible explanation for the rapid formation of δ′ precipitates in the as-quenched state [38]. Moreover, the typical core-shell β′/δ’ dispersoids were also observed in the matrix, which is due to the heterogeneous precipitation of δ′ on pre-existing β′ dispersoids

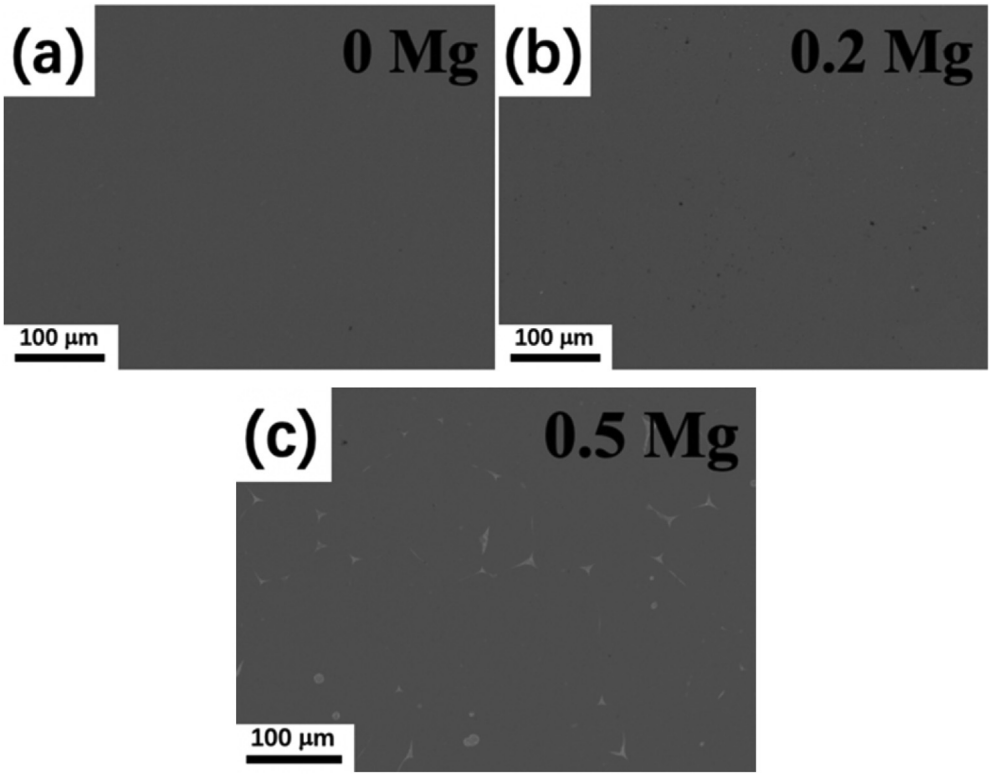

Fig. 5. SEM micrographs of Al–3Li–2Cu-xMg-0.15Zr alloys solution treated at 500 °C × 32 h + 560 °C × 24 h: (a) 0 Mg alloy, (b) 0.2 Mg alloy and (c) 0.5 Mg alloy.

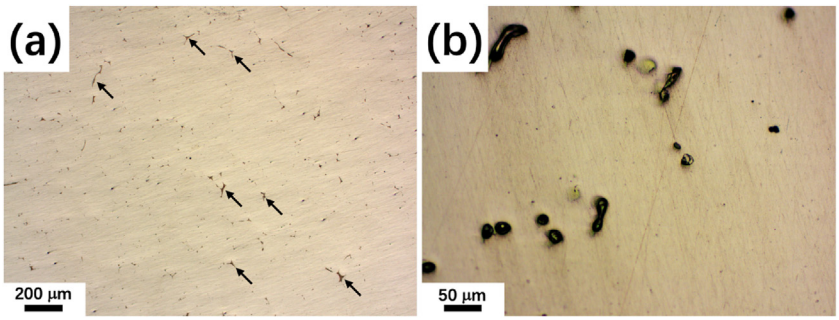

Fig. 6. (a) Optical microstructures of 0.5 Mg alloy solution treated at 500 °C × 36 h + 560 °C × 24 h + 570 °C × 12 h; (b) the enlarged image, indicating the occurrence of incipient melting.

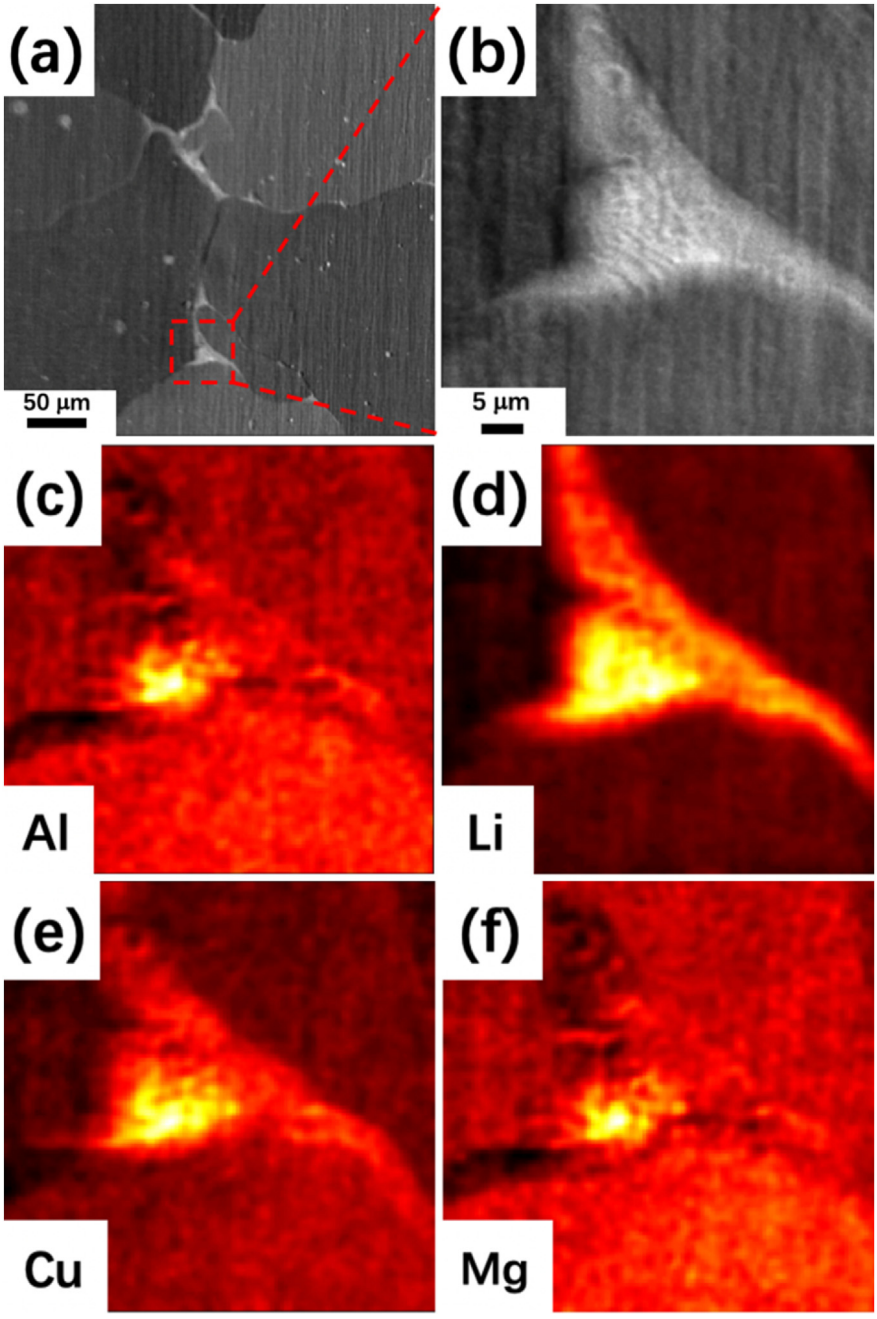

Fig. 7. XPS results of as-quenched 0.5 Mg alloy: (a) and (b) SEM micrographs; (c) the distribution of Al; (d) the distribution of Li; (e) the distribution of Cu; (f) the distribution of Mg. Brightness in (c–d) is proportional to the content.

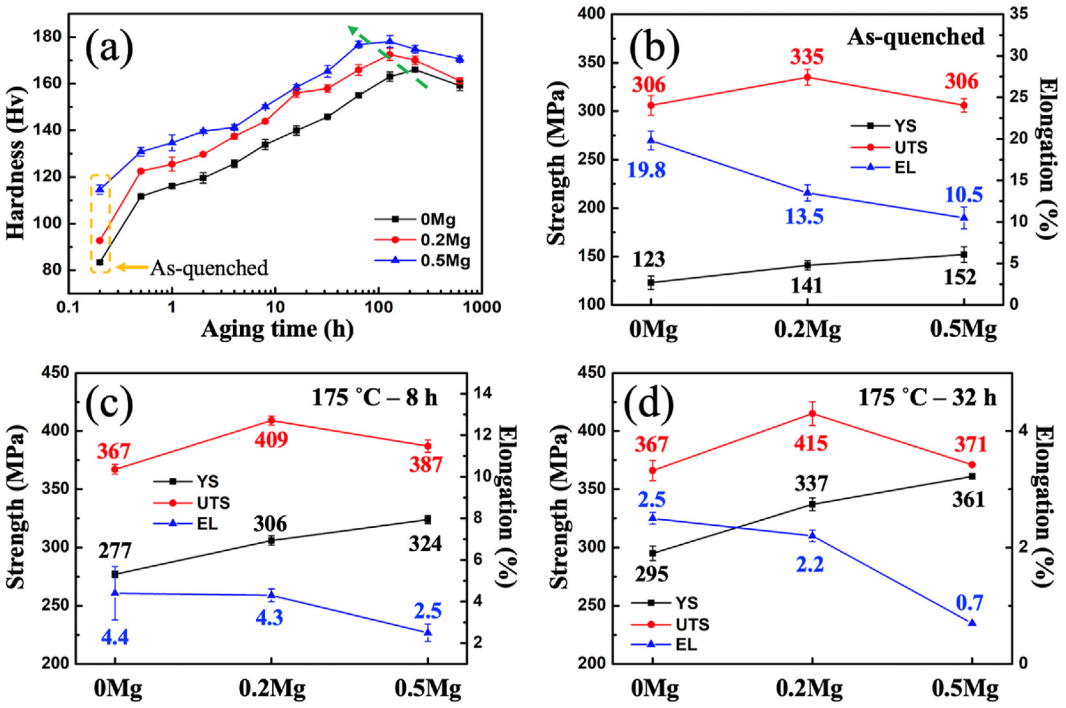

Fig. 8. (a) Vickers hardness evolution of the alloys during isothermal aging at 175 °C; (b)–(d) tensile test results at room temperature of the alloys in different states.

[39,40]. 0.2 Mg and 0.5 Mg alloys displayed a similar TEM micrograph in the AQ state (not given here), but it is impossible to confirm by the TEM micrographs whether the Mg atoms can accelerate the nucleation of δ′ phases or not, because of the extremely fine size and high number density of δ′ in the matrix. According to the literature [23], there may be strong interactions between Mg atoms and other solute atoms in the aluminum matrix, which will have a significant impact on the subsequent aging behavior. This is confirmed by the hardness evolution in Fig. 8a. Therefore, the 0.5 Mg alloy was selected for atom probe tomography (APT) analysis.

Fig. 10a displays the distribution of Li, Cu, and Mg atoms of the as-quenched 0.5 Mg alloy. It can be clearly seen that most of solutes atoms are randomly distributed, except for Li atoms, that is, fine δ′ precipitates observed in TEM micrograph. Fig. 10b shows the proximity histogram, revealing the solute concentrations across the Al matrix/δ′ interface. The average concentrations of Al and Li in the precipitate are 74.25 ± 1.13 at. % and 23.68 ± 1.16 at. % respectively, which is close to the stoichiometry ratio expected for Al_3Li. The average concentration of Mg in the matrix is similar to that in the precipitate and a negligible amount of Cu is present within the precipitate. In addition, the accumulation of Al and the depletion of Li on the matrix side of the α-Al/δ′ interface were observed. This effect was observed at all α-Al/δ′ interfaces, regardless of direction, and is likely kinetic in origin. During the growth of δ′ precipitates, Al atoms were continuously expelled from the particles, and Li atoms near the interface continued to diffuse into the particles. However, the long-range diffusion rate of atoms is relatively low compared with the short-range diffusion rate and the interface reaction rate, resulting in the accumulation of Al atoms and the depletion of Li atoms at the interface. Moreover, the radial distribution function (RDF) was used to describe the interactions between elements. The initial RDF value is greater than one in the case of positive correlation and is equal to one if there is no correlation between X and Y atoms

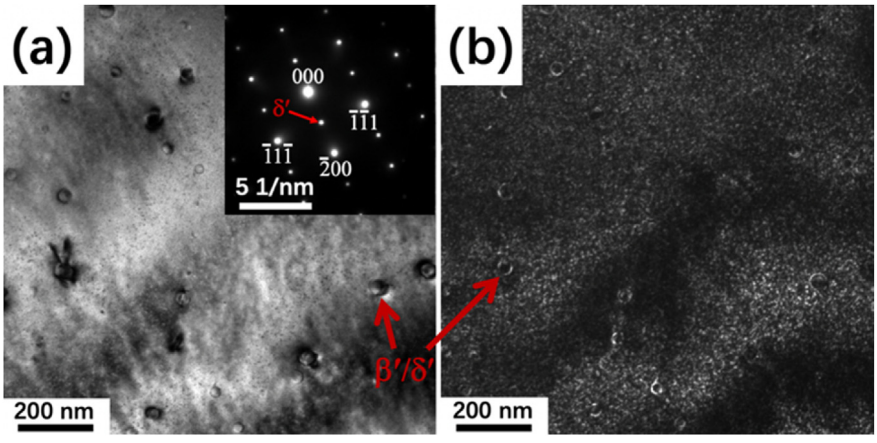

Fig. 9. TEM micrographs of 0 Mg alloy in AQ state: (a) bright-field (BF) micrograph; (b) dark-field (DF) micrograph.

[41]. In terms of 0.5 Mg alloy, the Cu–Mg cross-correlation and Mg–Mg autocorrelation shown in Fig. 10c are both positive and larger than unity, indicating that Mg and Cu atoms have a strong trend to form co-clusters. As is well documented in literature [42,43], Mg atoms in aluminum matrix preferentially combine with vacancies to form Mg-vacancy co-cluster, followed by gathering, which may result from high binding energy with vacancies and low diffusion activation energy of Mg atoms. Moreover, Mg atom also tends to form stable Mg–Cu bond, resulting in a large quantity of Mg–Cu-vacancy co-cluster, which is confirmed by the RDF results. The diffusion rate of these co-clusters is high, which may significantly promote the precipitation of the strengthening phase [17,44].

The bright-field (BF) and δ′-centered dark-field (δ′-CDF) micrographs of the three alloys in UA state are shown in Fig. 11. TEM micrographs of 0 Mg alloy, as shown in Fig. 11a and b, reveal that only some β′/δ’ precipitates and many δ′ precipitates existed within the matrix. Compared with the as-quenched samples, typical δ′ precipitates in all alloys after aging were obviously less in number density and greater in diameter. The addition of Mg element has significant influence on both kinetics and sequence of precipitation. Note that, other strengthening precipitates, such as θ′-Al_2Cu, T_1-Al_2CuLi, and S′-Al_2CuMg phases, can be distinguished according to their respective orientation relationships with the matrix, and the detailed descriptions of these precipitates also can be found in our previous work [15]. Apart from β′/δ’ and δ′ precipitates, many T_1 and θ′ plates were found in BF micrograph of 0.2 Mg alloy, as illustrated in Fig. 11c. Generally, in cast Al–Li–Cu alloys, especially those with high lithium content, the nucleation of T_1 and θ′ precipitates is difficult due to the extremely low density of dislocations, leading to a small amount of non-uniform distributed T_1 and θ′ precipitates in the matrix [11]. From inspection of Fig. 11a and c, the number density of θ′ and T_1 phases, especially θ′, increased markedly with more uniform distribution in 0.2 Mg alloy, which is inconsistent with the results of some reports [32]. Zhang and co-authors [32] indicated that the formation of θ′ precipitates would be suppressed by the addition of Mg. Note that, the content of Mg in 0.2 Mg alloy is smaller than that in the literature. This indicates that a small amount of Mg can play a significant effect, and slightly changing the content of Mg may cause tremendous changes. Combining the results of the above APT, we can infer that the formation of Cu-containing precipitates (T_1 and θ′) was accelerated by the Cu–Mg-vacancy co-clusters observed in the as-quenched state, which offered additional sites and diminished the energy barrier of these Cu-containing phases nucleation [17]. According to TEM micrographs, the notable enhancement in yield strength of 0.2 Mg alloy aged for 32 h was primarily because of the evolution of δ′ precipitates, while the formation of T_1 and θ′ precipitates provided additional strength increment. TEM micrographs of the 0.5 Mg alloy reveal that further increasing of the Mg content to 0.5 wt % encouraged the formation of S′ precipitates with lath-shaped morphology and suppressed the formation of T_1 and θ′ precipitates, as shown in Fig. 11e. S′ precipitates would compete with T_1 and θ′ precipitates for free heterogeneous nucleation sites and solute atoms in the α-Al matrix [24]. Besides, comparing Fig. 11c and e, it can be found that the nucleation and growth of S′ precipitate were accelerated at the expense of θ′ and T_1 precipitates. A large amount of uniformly distributed S′ precipitates is considered to enhance the plasticity and alleviate the anisotropy of mechanical properties by suppressing planar slip [45]. However, the distribution of S′ precipitates in 0.5 Mg alloy in UA state was uneven and sparse, which proved to provide a limited contribution to the enhancement of strength and ductility.

Based on the hardness evolution (Fig. 8a), Mg element shortened the time needed to obtain the peak-hardness from 268 h for 0 Mg alloy to 128 h for 0.5 Mg alloy. Fig. 12b, d, and f are the DF micrographs of 0 Mg, 0.2 Mg, and 0.5 Mg alloys, respectively, showing the further coarsening of δ′ precipitates in all the three alloys. In terms of 0 Mg alloy, many plate-like θ′ and T_1 precipitates with large aspect ratios were also identified in the matrix, as shown in Fig. 12a. The diffraction characteristics of θ′ precipitates were not found in the SAD pattern, indicating that the volume fraction of θ′ precipitates in the matrix is low. Note that, as marked in Fig. 12b, the preferential nucleation of δ′ precipitate on the broad and coherent interface between θ′ precipitates and the matrix was found, leading to the formation of “sandwich-like” δ′/θ’/δ′ phases. Fig. 12c is a BF

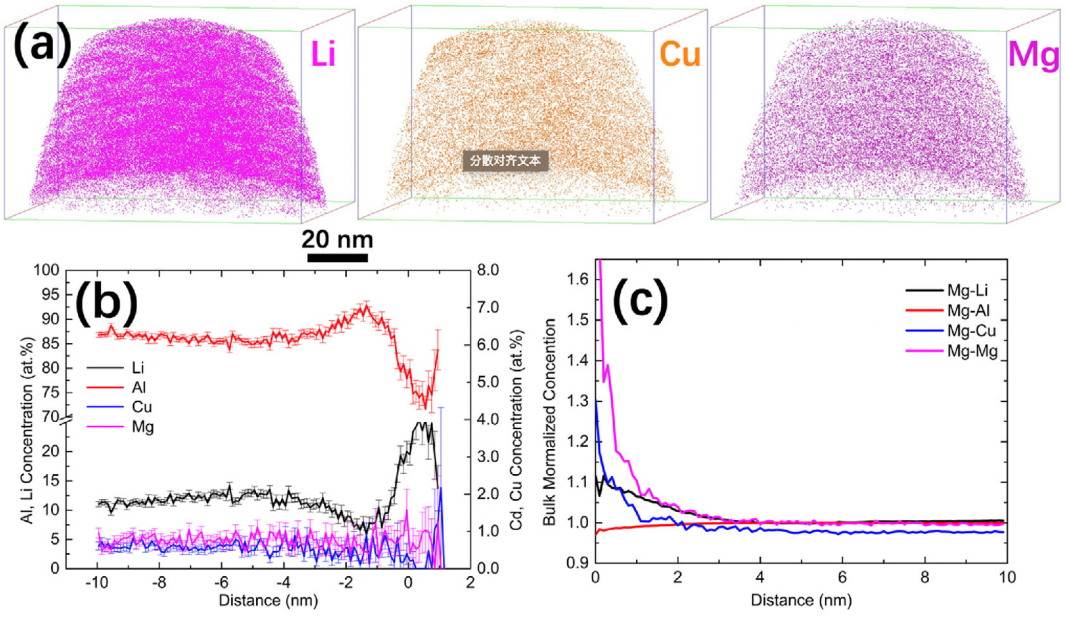

Fig. 10. APT results of the as-quenched 0.5 Mg alloy: (a) Atom maps of Li (Magenta), Cu (orange) and Mg (purple) atoms within the selected volume; (b) the proximity histogram profiles of the δ′ particle; (c) the radial distribution function (RDF) analysis results of Mg-x, Mg is the central atom. (For interpretation of the references to colour in this figure legend, the reader is referred to the Web version of this article.)

micrograph of 0.2 Mg alloy in PA state, which shows the thickness of T_1 precipitates formed on the $\{111\}_{Al}$ plane is extremely thin, and the morphology of T_1 precipitate shows no significant change, except for the rapid growth of diameter. Moreover, compared with the 0.2 Mg alloy in UA state, the number density of θ′ precipitate within the matrix significantly decreased, but its size increased. The most striking feature of 0.2 Mg alloy in PA state is the formation of a large number of S′ precipitates. Comparing between the microstructure of 0 Mg alloy and that of 0.2 Mg alloy, the number density of T_1 precipitate in the latter is significantly larger than that in the former, and the average size is smaller in the latter, indicating that minor Mg atoms could significantly promote the formation of T_1 precipitates and effectively inhibits its growth rate. Fig. 12e displays the BF micrographs of 0.5 Mg alloy in PA state. Compared with the UA state (Fig. 11e), the formation and growth of S′ precipitate were accompanied by the formation of a large amount of T_1 precipitates, which can be proved by the SAD pattern inset in Fig. 12e. However, no θ′ precipitate was observed within matrix, or its volume fraction was

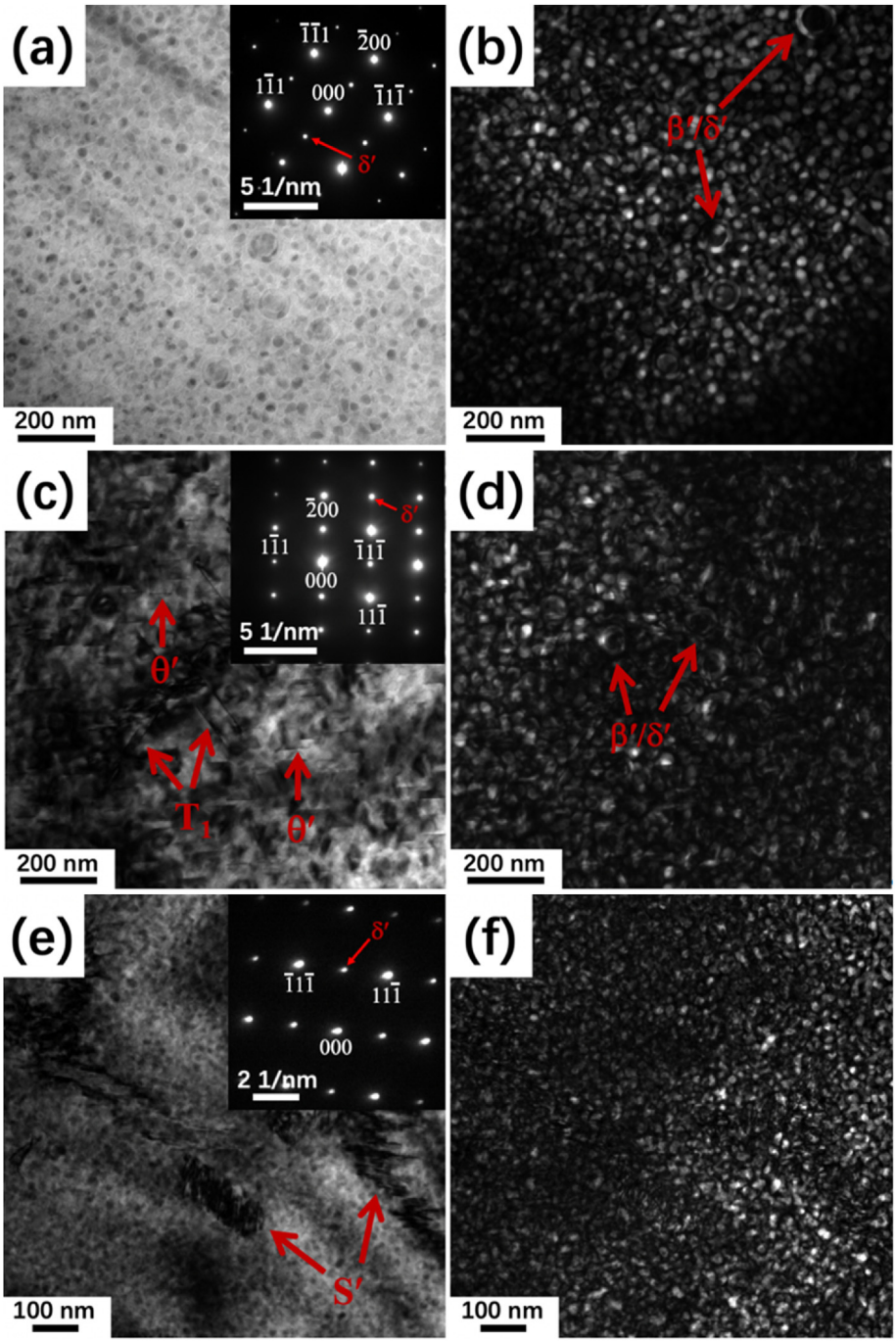

Fig. 11. TEM micrographs of the three alloys in UA state: (a) BF micrograph and SAD pattern viewed along $[011]_{Al}$ zone axis of 0 Mg alloy; (b) the corresponding DF micrograph of 0 Mg alloy; (c) BF micrograph and SAD pattern viewed along $[011]_{Al}$ zone axis of 0.2 Mg alloy; (d) the corresponding DF micrograph of 0.2 Mg alloy; (e) BF micrograph and SAD pattern viewed along $[011]_{Al}$ zone axis of 0.5 Mg alloy; (f) the corresponding DF micrograph of 0.5 Mg alloy.

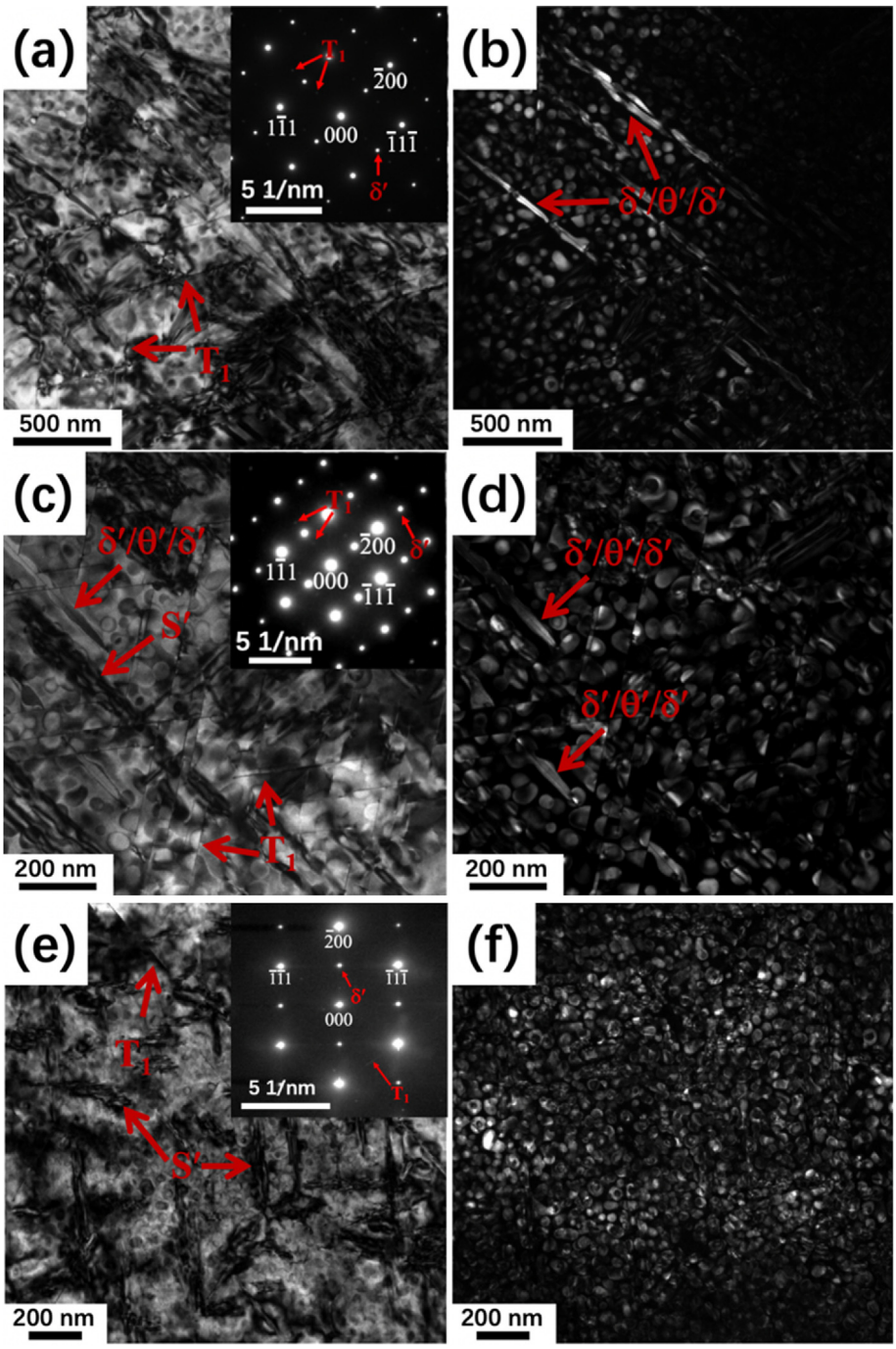

Fig. 12. TEM micrographs of the three alloys in PA state: (a) BF micrograph and SAD pattern viewed along $[011]_{Al}$ zone axis of 0 Mg alloy; (b) the corresponding DF micrograph of 0 Mg alloy; (c) BF micrograph and SAD pattern viewed along $[011]_{Al}$ zone axis of 0.2 Mg alloy; (d) the corresponding DF micrograph of 0.2 Mg alloy; (e) BF micrograph and SAD pattern viewed along $[011]_{Al}$ zone axis of 0.5 Mg alloy; (f) the corresponding DF micrograph of 0.5 Mg alloy.

extremely low, which matches well with the results in other reports [46]. The balance of competitive precipitation between θ′ and S′ phases is dominated by the content of Mg. When the content of Mg in the alloy exceeds 0.5 wt %, the formation of θ′ precipitate will be significantly hindered, leading to the predominance of S′ and T_1 precipitates in the matrix. Moreover, the formation of T_1 precipitate is also retarded when the content of Mg increases from 0.2 to 0.5 wt % since the number density and the average size of T_1 precipitate in 0.5 Mg alloy are lower and smaller than those of T_1 precipitate in 0.2 Mg alloy at the same aging time.

Fig. 13 displays TEM micrographs of the three alloys in OA state. In addition to the coarsening of δ′ precipitate, the lengthening of T_1 precipitates and the coarsening of θ′ precipitates were observed as well in 0 Mg alloy. Generally, T_1 precipitate is usually extremely thin, ~1.3 nm in thickness, which is approximately five times the {111} spacing of Al, and it was recognized that the thickness of T_1 precipitate is very stable at ~170 °C [47]. Fig. 13c is a BF micrograph of 0.2 Mg alloy in OA state, indicating the existence of numerous T_1 and "sandwich-like" δ′/θ′/δ′ precipitates with immensely increased aspect ratio. The 0.2 Mg alloy in OA state was characterized by predominant T_1, S′, "sandwich-like" δ′/θ′/δ′ and δ′ precipitates. Note that, the thickness of θ′ precipitates in 0 Mg and 0.2 Mg alloys in OA

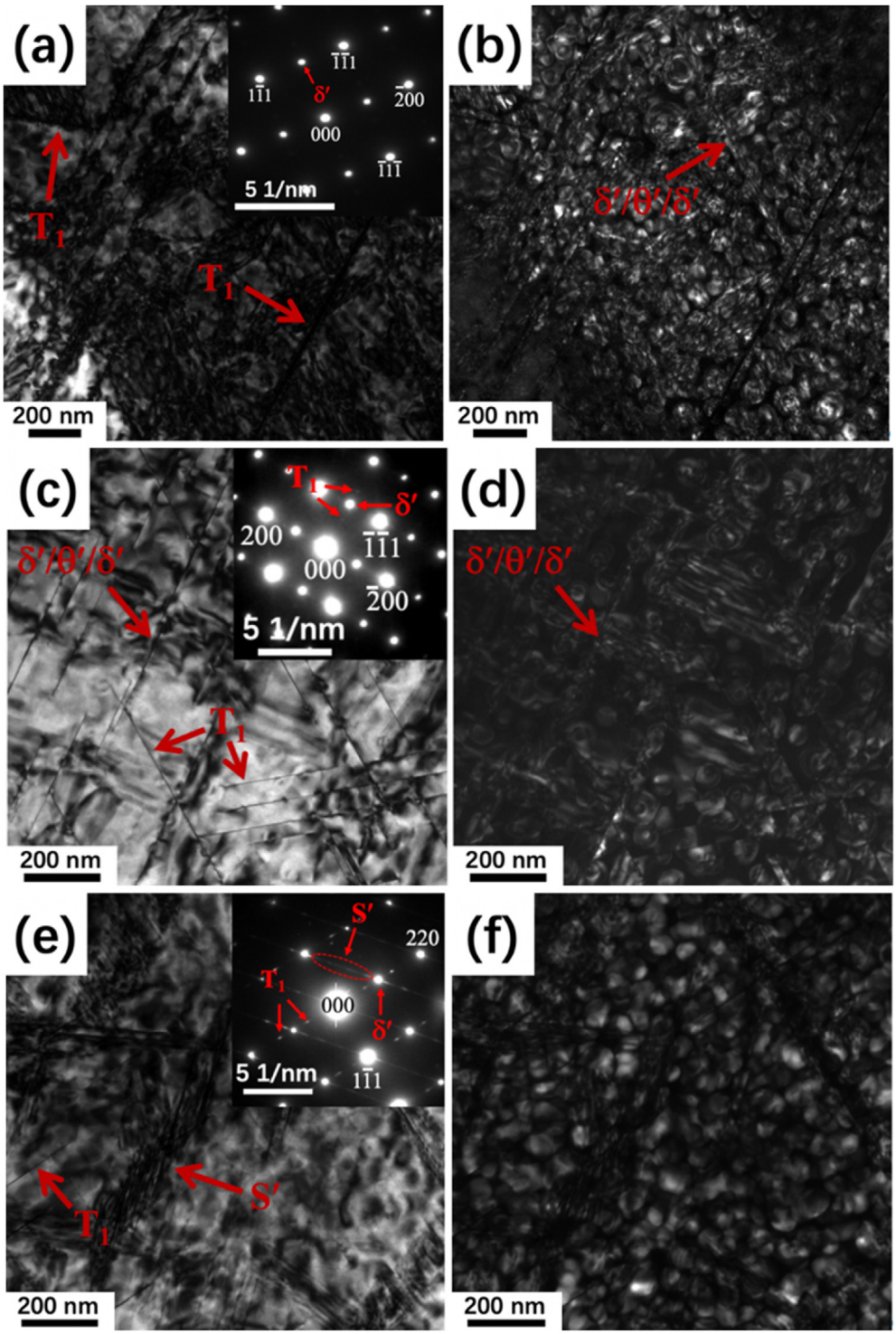

Fig. 13. TEM micrographs of the three alloys in OA state: (a) BF micrograph and SAD pattern viewed along $[011]_{Al}$ zone axis of 0 Mg alloy; (b) the corresponding DF micrograph of 0 Mg alloy; (c) BF micrograph and SAD pattern viewed along $[011]_{Al}$ zone axis of 0.2 Mg alloy; (d) the corresponding DF micrograph of 0.2 Mg alloy; (e) BF micrograph and SAD pattern viewed along $[12]_{Al}$ zone axis of 0.5 Mg alloy; (f) the corresponding DF micrograph of 0.5 Mg alloy.

state is much smaller than that in other conventional cast Al—Cu alloys. As well known, the lenticular δ′ precipitates nucleated heterogeneously on the two sides of θ′ precipitate can inhibit the coarsening of θ′ precipitate during isothermal aging and effectively ameliorate the microstructure stability [48]. Fig. 13e shows the BF micrograph of 0.5 Mg alloy in OA state displaying the existence of T_1 precipitate and coarsened S′ precipitates. The lengthening rate of T_1 precipitate in 0.5 Mg alloy is slower than that in the 0 Mg alloy, which may be due to the competitive precipitation with S′ and the suppressed coarsening rate of δ′.

Table 2 lists the main precipitates of the three alloys in different aging states. Mg element has a noticeable impact on the kinetics and sequence of precipitation. Minor Mg addition (0.2 wt %) can accelerate the diffusion of Cu atoms [23], thereby promoting the

Table 2
Predominant precipitates of Al−3Li−2Cu-xMg-0.15Zr alloys in different aging states.

Condition	Predominant precipitates after ageing at 175 °C		
	0 Mg	0.2 Mg	0.5 Mg
As-quenched	δ′	δ’	δ′
Under-aged	δ′	δ’, T_1, θ′	δ’, S′
Peak-aged	δ′, T_1, δ′/θ’/δ′	δ’, T_1, δ′/θ’/δ′, S′	δ’, T_1, S′
Over-aged	δ′, T_1, δ′/θ’/δ′	δ’, T_1, δ′/θ’/δ′, S′	δ’, T_1, S′

nucleation of the T_1 and θ′ precipitates. With further increasing the content of Mg to 0.5 wt %, many Mg−Cu-vacancy co-clusters formed in the matrix are more likely to be converted to S′ precipitates. Since the nucleation and growth of S′ precipitates consume a large number of Cu atoms, the nucleation and growth of T_1 and θ′ precipitates would be significantly suppressed. Unfortunately, the distribution of S′ precipitates in the matrix of the two Mg-containing alloys is uneven as a result of the low number of heterogeneous nucleation sites, indicating that increasing Mg content cannot promote the homogeneous nucleation of S′ precipitate, which is consistent with previous report [32].

3.5. Evolution of δ′-precipitation-free zones (δ′-PFZ)

Fig. 14 displays the evolution of δ′-precipitate-free zones (δ′-PFZs) of the three alloys in different aging states. The half width of δ′-PFZs is defined as the distance from the grain boundary to the nearest δ′ precipitate. No obvious δ′-PFZs was observed in all the as-quenched alloys, hence it is assumed that the half width of δ′-PFZs in the as-quenched state is zero. The mean half width of δ′-PFZs in all the three alloys increased significantly along with the aging process, accompanied by gradual dissolution and continuous coarsening of δ′ precipitates near the grain boundary. Note that, the coarsening rate of δ′-PFZs in two Mg-containing alloys is lower than that in 0 Mg alloy, and the coarsening rate further decreases as the Mg content increases. This indicates that Mg element can inhibit the coarsening of δ′-PFZs. At present, Mg may decrease the coarsening rate of δ′-PFZs through the following mechanisms: (1) The high binding energy of Mg atoms and vacancies [49] inhibits the diffusion of Li atoms, thereby reducing the growth of δ′ precipitates and δ′-PFZs; (2) Mg atoms combine with vacancies to form co-clusters, which is conducive to the stability of vacancies and inhibits their diffusion to annihilate at the grain boundary [50,51], thus ensuring that there is

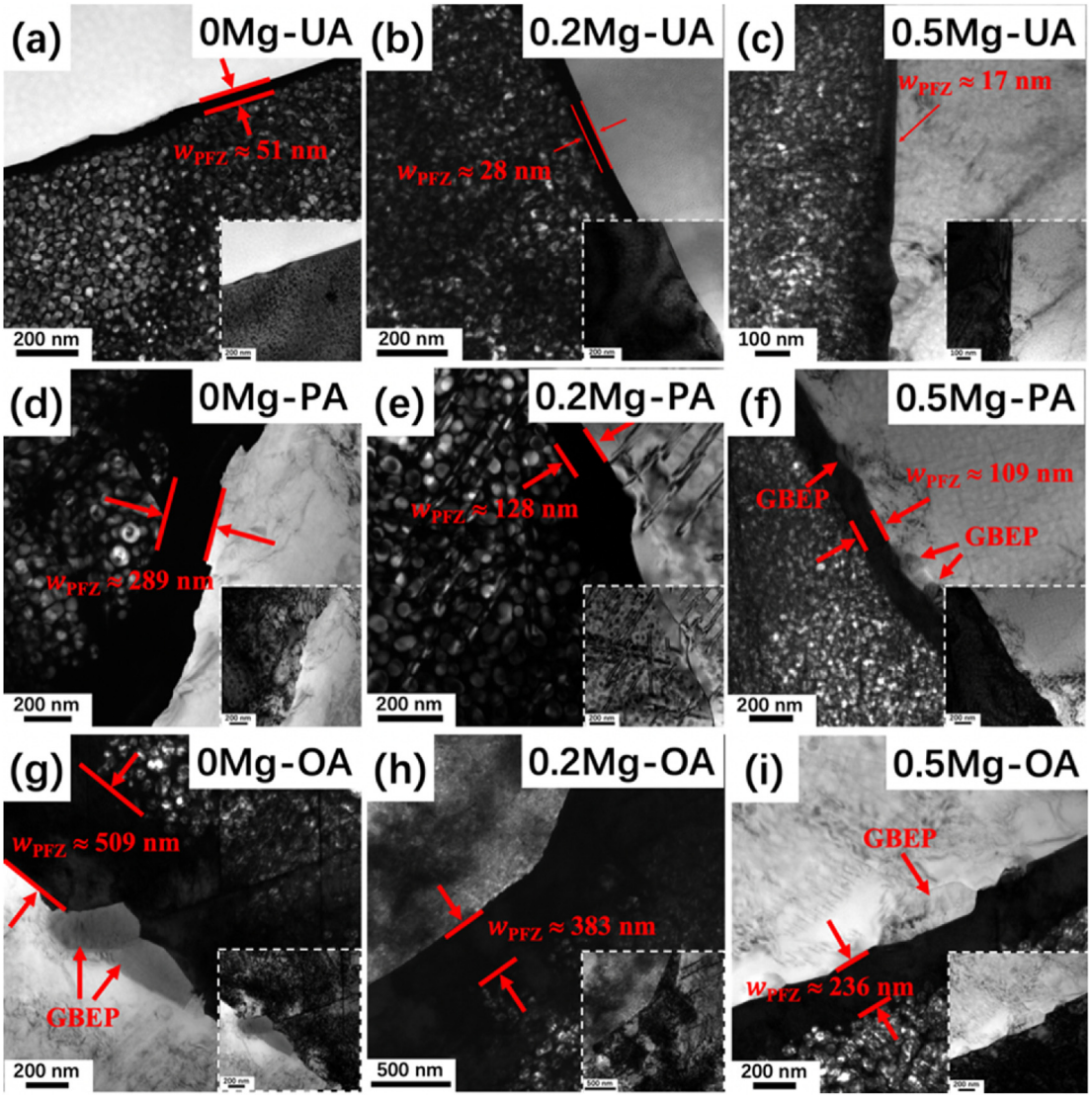

Fig. 14. Evolution of δ′-precipitation-free zones near the grain boundary: (a), (b) and (c) TEM micrographs of 0 Mg, 0.2 Mg and 0.5 Mg alloys in UA state; (d), (e) and (f) TEM micrographs of 0 Mg, 0.2 Mg and 0.5 Mg alloys in PA state; (g), (h) and (i) TEM micrographs of 0 Mg, 0.2 Mg and 0.5 Mg alloys in OA state.

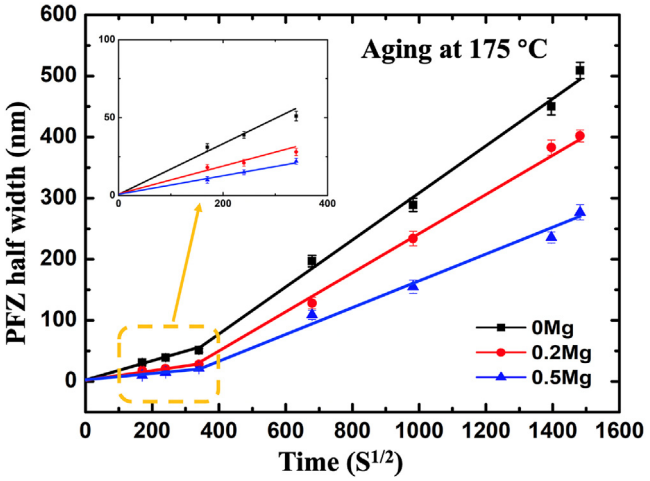

Fig. 15. The measured half width of δ′-PFZs in 0 Mg, 0.2 Mg, and 0.5 Mg alloys drawn as a function of aging time (The independent variable is the square root of aging time, $t^{1/2}$). The linear fitting lines obtained by linear regression analysis are also plotted in the figure.

still enough vacancy concentration near the grain boundary to meet the critical nucleation requirements. It is generally believed that the δ′-PFZs is harmful to the ductility of the alloy [52], so reducing the width of the δ′-PFZs is beneficial to improving the performance of the alloy.

There are two main viewpoints on the formation mechanism of δ′-PFZs: one is the vacancy-depletion mechanism, and the other is the solute-depletion mechanism [53]. Vacancy-depletion mechanism: this mechanism believes that a large number of vacancies generated during quenching tend to diffuse to the grain boundary and annihilate in the subsequent aging process, resulting in a significant decrease in the concentration of vacancies. When the concentration of vacancies near the grain boundary is lower than the critical value, the δ′ precipitates cannot nucleate, thereby forming δ′-precipitate-free zones. Solute-depletion mechanism: the nucleation and growth of grain boundary equilibrium phases (GBEPs) result in massive consumption of solute atoms near the grain boundary. When the concentration of solute atoms is smaller than the critical value required for δ′ precipitate nucleation, the δ′ precipitates cannot nucleate neither, thereby forming δ′-precipitate-free zones. Jha and Sanders et al. [54] proposed the following equation based on the solute-depletion mechanism to describe the evolution law of the width of δ′-PFZs with aging time:where is the half width of δ′-PFZs, is the growth rate constant and is aging time.

Fig. 15 displays the measured half width of δ′-PFZs as a function of aging time for the three alloys. The lines obtained by linear regression analysis were also superimposed on the figure. The most striking feature of the evolution of the half width of δ′-PFZs is that the fitting curves of all the three alloys are composed of two straight lines with different slopes, which is inconsistent with previous reports [54,55]. In all the three alloys, the slope of the linear fitting line before 32 h is significantly lower than that after 32 h. This indicates that the evolution of δ′-PFZs is not solely determined by the solute-depletion mechanism, but may involve the transformation of two different formation mechanisms. In fact, no GBEPs was observed near the grain boundary in the UA state (Fig. 14a–c), and coarse GBEPs was one of the main characteristics of the grain boundary in PA and OA states, as indicated in Fig. 14f, g, and i. In summary, it can be speculated that the initial formation mechanism of δ′-PFZs is mainly the vacancy-depletion mechanism. With the nucleation and growth of the GBEPs, the evolution of δ′-PFZs is mainly determined by the solute-depletion mechanism in the middle and late stage of aging. It is worth mentioning that in both stages, Mg element can significantly reduce the slope of the linear fitting lines, indicating that Mg can not only suppress the annihilation of vacancies at grain boundaries but also reduce the diffusion rate of Li atoms.

4. Conclusions

The impact of minor Mg addition on microstructural evolution and comprehensive mechanical performance of cast Al–3Li–2Cu-0.15Zr alloy was studied. The principal findings are as follows:

1. Raising Mg content gradually altered the microstructure of the as-cast alloys and increased the volume fraction and types of grain boundary intermetallic phases.
2. The initial melting temperature of the alloys was not affected by Mg element, but a (Li, Cu, Mg)-rich intermetallic phase was observed in the 0.5 Mg alloy. This quaternary phase is extremely difficult to dissolve into the matrix during heat treatment, and the distribution of solute elements within this phase is uneven, resulting in the inability to identify its type. Unusually, the solvus temperature is higher than the solidus temperature in the 0.5 Mg alloy, resulting in the incipient melting in the matrix before the complete dissolution of the intermetallic phases.
3. The hardness of the alloys in the as-quenched state increased with increasing the content of Mg, as a result of solid solution strengthening of Mg atoms and the improved formation of δ′ precipitate. Prominent enhancements in both age-hardening and precipitation kinetics of the base alloy with minor Mg addition were clearly observed.
4. Mg element has a remarkable impact on precipitation behavior, including the sequence and kinetics of solid-state precipitation, during isothermal aging. Minor Mg addition (0.2 wt %) could encourage the diffusion of Cu atoms by the aggregation of Mg–Cu-vacancy co-clusters, thereby promoting the nucleation of the T_1 and θ′ precipitates. In addition, S′ precipitate was therefore introduced as a result of Mg addition. Further increasing the content of Mg to 0.5 wt %, the nucleation and growth of S′ precipitates would be promoted at the expense of T_1 and θ′ precipitates, especially θ′ precipitate.
5. Based on the theoretical models and regression analysis, it can be inferred that the initial formation mechanism of δ′-PFZs is mainly the vacancy-depletion mechanism. The evolution of δ′-PFZs is mainly determined by the solute-depletion mechanism in the middle and late stage of aging, with the nucleation and growth of the GBEPs. Since Mg atoms can not only suppress the annihilation of vacancies at grain boundaries but also reduce the diffusion rate of Li atoms, the addition of Mg element can significantly inhibit the coarsening of δ′-PFZs.
6. The best balance between strength (UTS = 415 MPa, YS = 337 MPa) and ductility (EL = 2.2%) was obtained by 0.2 Mg alloy aged at 175 °C for 32 h. In addition, 0.2 Mg alloy also has significant advantages in terms of density (2.437 g/cm^3) and elastic modulus (82.65 GPa) over conventional cast aluminum alloys (density: 2.7–2.8 g/cm^3; elastic modulus: 72 GPa).

Data availability

The raw/processed data required to reproduce these findings cannot be shared at this time as the data also forms part of an ongoing study.

CRediT authorship contribution statement

Liang Wu: Conceptualization, Investigation, Data curation, Formal analysis, Methodology, Visualization, Writing - original draft. **Xianfeng Li:** Conceptualization, Data curation, Validation, Writing - review & editing. **Haowei Wang:** Data curation, Resources, Methodology, Supervision.

Declaration of competing interest

The authors declare that they have no known competing financial interests or personal relationships that could have appeared to influence the work reported in this paper.

Acknowledgments

L. Wu is grateful for the scholarship supported by the China Scholarship Council (Grant no. 201906230200). The authors would like to thank Dr. Yugang Li at Shanghai Jiao Tong University for assistance.

References

[1] J.C. Williams, E.A. Starke Jr., Progress in structural materials for aerospace systems, Acta Mater. 51 (2003) 5775–5799, https://doi.org/10.1016/j.actamat.2003.08.023.
[2] A. Deschamps, C. Sigli, T. Mourey, F. De Geuser, W. Lefebvre, B. Davo, Experimental and modelling assessment of precipitation kinetics in an Al–Li–Mg alloy, Acta Mater. 60 (2012) 1917–1928, https://doi.org/10.1016/j.actamat.2012.01.010.
[3] S.J. Kang, T.-H. Kim, C.-W. Yang, J.I. Lee, E.S. Park, T.W. Noh, M. Kim, Atomic structure and growth mechanism of T_1 precipitate in Al–Cu–Li–Mg–Ag alloy, Scripta Mater. 109 (2015) 68–71, https://doi.org/10.1016/j.scriptamat.2015.07.020.
[4] R.J. Rioja, Fabrication methods to manufacture isotropic Al-Li alloys and products for space and aerospace applications, Mater. Sci. Eng., A 257 (1998) 100–107, https://doi.org/10.1016/S0921-5093(98)00827-2.
[5] E. Starke, T. Sanders, I. Palmer, New approaches to alloy development in the Al-Li system, JOM (J. Occup. Med.) 33 (1981) 24–33, https://doi.org/10.1007/BF03339468.
[6] R.J. Rioja, J. Liu, The evolution of Al-Li base products for aerospace and space applications, Metall. Mater. Trans. A 43 (2012) 3325–3337, https://doi.org/10.1007/s11661-012-1155-z.
[7] E. Gumbmann, F. De Geuser, C. Sigli, A. Deschamps, Influence of Mg, Ag and Zn minor solute additions on the precipitation kinetics and strengthening of an Al-Cu-Li alloy, Acta Mater. 133 (2017) 172–185, https://doi.org/10.1016/j.actamat.2017.05.029.
[8] B. Gable, A. Zhu, A. Csontos, E. Starke Jr., The role of plastic deformation on the competitive microstructural evolution and mechanical properties of a novel Al–Li–Cu–X alloy, J. Light Met. 1 (2001) 1–14, https://doi.org/10.1016/S1471-5317(00)00002-X.
[9] L. Wu, X. Li, G. Han, Y. Deng, N. Ma, H. Wang, Precipitation behavior of the high-Li-content in-situ TiB_2/Al-Li-Cu composite, Mater. Char. 132 (2017) 215–222, https://doi.org/10.1016/j.matchar.2017.08.015.
[10] B. Gault, X.Y. Cui, M.P. Moody, F. De Geuser, C. Sigli, S.P. Ringer, A. Deschamps, Atom probe microscopy investigation of Mg site occupancy within δ′ precipitates in an Al–Mg–Li alloy, Scripta Mater. 66 (2012) 903–906, https://doi.org/10.1016/j.scriptamat.2012.02.021.
[11] L. Wu, C. Zhou, X. Li, N. Ma, H. Wang, Effects of TiB_2 particles on artificial aging response of high-Li-content TiB_2/Al-Li-Cu composite, J. Alloys Compd. 749 (2018) 189–196, https://doi.org/10.1016/j.jallcom.2018.03.299.
[12] B. Pletcher, K. Wang, M. Glicksman, Experimental, computational and theoretical studies of δ′ phase coarsening in Al–Li alloys, Acta Mater. 60 (2012) 5803–5817, https://doi.org/10.1016/j.actamat.2012.07.021.
[13] E.J. Lavernia, N.J. Grant, Aluminium-lithium alloys, J. Mater. Sci. 22 (1987) 1521–1529, https://doi.org/10.1007/BF01132370.
[14] A. Il'in, S. Nikitin, O. Osintsev, Y.V. Borisov, Effect of alloying elements on the structure and properties of Al-Li-Cu cast alloys, Russ. Metall. 4 (2009) 338–344, https://doi.org/10.1134/S0036029509040107.
[15] L. Wu, C. Zhou, X. Li, N. Ma, H. Wang, Microstructural evolution and mechanical properties of cast high-Li-content TiB_2/Al-Li-Cu composite during heat treatment, J. Alloys Compd. 739 (2018) 270–279, https://doi.org/10.1016/j.jallcom.2017.12.126.
[16] K. Kumar, F. Heubaum, The effect of Li content on the natural aging response of Al-Cu-Li-Mg-Ag-Zr alloys, Acta Mater. 45 (1997) 2317–2327, https://doi.org/10.1016/S1359-6454(96)00360-6.
[17] S. Hirosawa, T. Sato, A. Kamio, Effects of Mg addition on the kinetics of low-temperature precipitation in Al–Li–Cu–Ag–Zr alloys, Mater. Sci. Eng., A 242 (1998) 195–201, https://doi.org/10.1016/S0921-5093(97)00530-3.
[18] L. Wu, Y. Li, X. Li, N. Ma, H. Wang, Interactions between cadmium and multiple precipitates in an Al-Li-Cu alloy: improving aging kinetics and precipitation hardening, J. Mater. Sci. Technol. 46 (2020) 44–49, https://doi.org/10.1016/j.jmst.2019.11.032.
[19] G. Itoh, Q. Cui, M. Kanno, Effects of a small addition of magnesium and silver on the precipitation of T_1 phase in an Al-4%Cu-1.1%Li-0.2%Zr alloy, Mater. Sci. Eng., A 211 (1996) 128–137, https://doi.org/10.1016/0921-5093(95)10157-8.
[20] K. Kumar, S. Brown, J.R. Pickens, Microstructural evolution during aging of an Al-Cu-Li-Ag-Mg-Zr alloy, Acta Mater. 44 (1996) 1899–1915, https://doi.org/10.1016/1359-6454(95)00319-3.
[21] W. Cassada, G. Shiflet, E. Starke, Mechanism of Al_2CuLi (T_1) nucleation and growth, Metall. Trans. A 22 (1991) 287–297, https://doi.org/10.1007/BF02656798.
[22] W. Cassada, G. Shiflet, E. Starke, The effect of plastic deformation on Al_2CuLi (T_1) precipitation, Metall. Trans. A 22 (1991) 299–306, https://doi.org/10.1007/BF02656799.
[23] L. Wu, Y. Chen, X. Li, N. Ma, H. Wang, Rapid hardening during natural aging of Al-Cu-Li based alloys with Mg addition, Mater. Sci. Eng., A 743 (2019) 741–744, https://doi.org/10.1016/j.msea.2018.11.119.
[24] J. Kim, J.K. Park, Effect of stretching on the precipitation kinetics of an Al-2.0Li-2.8Cu-0.5Mg (-0.13Zr) alloy, Metall. Mater. Trans. A 24 (1993) 2613–2621, https://doi.org/10.1007/BF02659485.
[25] D. Tsivoulas, J. Robson, Heterogeneous Zr solute segregation and Al_3Zr dispersoid distributions in Al–Cu–Li alloys, Acta Mater. 93 (2015) 73–86, https://doi.org/10.1016/j.actamat.2015.03.057.
[26] K. Baveja, Dynamic method of measuring Young's modulus of elasticity, J. Sci. Instrum. 41 (1964) 662–665, https://doi.org/10.1088/0950-7671/41/11/302.
[27] A. Chen, G. Wu, L. Zhang, X. Zhang, C. Shi, Y. Li, Microstructural characteristics and mechanical properties of cast Al-3Li-xCu-0.2 Zr alloy, Mater. Sci. Eng., A 677 (2016) 29–40, https://doi.org/10.1016/j.msea.2016.09.040.
[28] A. Mukhopadhyay, D. Zhou, Q. Yang, Effect of variation in the Cu: Mg ratios on the formation of T_2 and C phases in AA 8090 alloys, Scripta Metall. Mater. 26 (1992) 237–242, https://doi.org/10.1016/0956-716X(92)90179-I.
[29] J.-M. Kim, K.-D. Seong, J.-H. Jun, K. Shin, K.-T. Kim, W.-J. Jung, Microstructural characteristics and mechanical properties of Al–2.5 wt.% Li–1.2 wt.% Cu–xMg alloys, J. Alloys Compd. 434 (2007) 324–326, https://doi.org/10.1016/j.jallcom.2006.08.230.
[30] I. Fridlyander, L. Rokhlin, T. Dobatkina, N. Nikitina, Investigation of the phase equilibria in aluminum alloys containing lithium, Met. Sci. Heat Treat. 35 (1993) 567–571, https://doi.org/10.1007/BF00778667.
[31] S. Nikitin, O. Osintsev, S.Y. Betsofen, Effect of heat treatment conditions on the structure and mechanical properties of a cast Al-Li-Cu aluminum alloy, Russ. Metall. 11 (2010) 1041–1045, https://doi.org/10.1134/S003602951011008X.
[32] X. Zhang, L. Zhang, G. Wu, C. Shi, J. Zhang, Influences of Mg content on the microstructures and mechanical properties of cast Al–2Li–2Cu–0.2 Zr alloy, J. Mater. Sci. 54 (2019) 791–811, https://doi.org/10.1007/s10853-018-2826-y.
[33] F. Wang, Z. Liu, D. Qiu, J.A. Taylor, M.A. Easton, M.-X. Zhang, Revisiting the role of peritectics in grain refinement of Al alloys, Acta Mater. 61 (2013) 360–370, https://doi.org/10.1016/j.actamat.2012.09.075.
[34] Y. Liu, Z. Hu, Y. Zhang, C. Shi, The solidification behavior of 8090 Al-Li alloy, Metall. Trans. B 24 (1993) 857–865, https://doi.org/10.1007/BF02663146.
[35] R. Dorward, Solidus and solvus isotherms for quaternary Al-Li-Cu-Mg alloys, Metall. Trans. A 19 (1988) 1631–1634, https://doi.org/10.1007/BF02674041.
[36] R. Yoshimura, T.J. Konno, E. Abe, K. Hiraga, Transmission electron microscopy study of the early stage of precipitates in aged Al–Li–Cu alloys, Acta Mater. 51 (2003) 2891–2903, https://doi.org/10.1016/S1359-6454(03)00104-6.
[37] K. Hono, S. Babu, K. Hiraga, R. Okano, T. Sakurai, Atom probe study of early stage phase decomposition in an Al-7.8 at.%Li alloy, Acta Metall. Mater. 40 (1992) 3027–3034, https://doi.org/10.1016/0956-7151(92)90466-R.
[38] V. Radmilovic, A. Fox, G. Thomas, Spinodal decomposition of Al-rich Al-Li alloys, Acta Metall. 37 (1989) 2385–2394, https://doi.org/10.1016/0001-6160(89)90036-9.
[39] F.W. Gayle, J.B. Vander Sande, "Composite" precipitates in an Al-Li-Zr alloy, Scripta Metall. 18 (1984) 473–478, https://doi.org/10.1016/0036-9748(84)90424-1.
[40] H. Flower, P. Gregson, Solid state phase transformations in aluminium alloys containing lithium, Mater. Sci. Technol. 3 (1987) 81–90, https://doi.org/10.1179/mst.1987.3.2.81.
[41] F. De Geuser, W. Lefebvre, D. Blavette, 3D atom probe study of solute atoms clustering during natural ageing and pre-ageing of an Al-Mg-Si alloy, Phil. Mag. Lett. 86 (2006) 227–234, https://doi.org/10.1080/09500830600643270.
[42] Y. Nagai, M. Murayama, Z. Tang, T. Nonaka, K. Hono, M. Hasegawa, Role of vacancy–solute complex in the initial rapid age hardening in an Al–Cu–Mg alloy, Acta Mater. 49 (2001) 913–920, https://doi.org/10.1016/S1359-6454(00)00348-7.
[43] A. Charai, T. Walther, C. Alfonso, A.-M. Zahra, C. Zahra, Coexistence of clusters, GPB zones, S″-, S′-and S-phases in an Al–0.9%Cu–1.4%Mg alloy, Acta Mater. 48 (2000) 2751–2764, https://doi.org/10.1016/S1359-6454(99)00422-X.
[44] S. Ringer, K. Hono, I. Polmear, T. Sakurai, Nucleation of precipitates in aged Al-Cu-Mg-(Ag) alloys with high Cu:Mg ratios, Acta Mater. 44 (1996) 1883–1898, https://doi.org/10.1016/1359-6454(95)00314-2.
[45] P. Gregson, H. Flower, Microstructural control of toughness in aluminium-lithium alloys, Acta Metall. 33 (1985) 527–537, https://doi.org/10.1016/0001-6160(85)90095-1.

[46] X. Zhang, L. Zhang, G. Wu, W. Liu, C. Shi, J. Tao, J. Sun, Microstructural evolution and mechanical properties of cast Al-2Li-2Cu-0.5 Mg-0.2 Zr alloy during heat treatment, Mater. Char. 132 (2017) 312–319, https://doi.org/10.1016/j.matchar.2017.08.027.
[47] A. Deschamps, B. Decreus, F. De Geuser, T. Dorin, M. Weyland, The influence of precipitation on plastic deformation of Al–Cu–Li alloys, Acta Mater. 61 (2013) 4010–4021, https://doi.org/10.1016/j.actamat.2013.03.015.
[48] S. Duan, C. Wu, Z. Gao, L. Cha, T. Fan, J. Chen, Interfacial structure evolution of the growing composite precipitates in Al-Cu-Li alloys, Acta Mater. 129 (2017) 352–360, https://doi.org/10.1016/j.actamat.2017.03.018.
[49] C. Beatrice, W. Garlipp, M. Cilense, A. Adorno, Vacancy-Mg atom binding energy in Al-Mg alloys, Scripta Metall. Mater. 32 (1995) 23–26, https://doi.org/10.1016/S0956-716X(99)80005-3.
[50] R.K. Marceau, G. Sha, R. Ferragut, A. Dupasquier, S. Ringer, Solute clustering in Al–Cu–Mg alloys during the early stages of elevated temperature ageing, Acta Mater. 58 (2010) 4923–4939, https://doi.org/10.1016/j.actamat.2010.05.020.
[51] F.W. Gayle, F.H. Heubaum, J.R. Pickens, Structure and properties during aging of an ultra-high strength Al-Cu-Li-Ag-Mg alloy, Scripta Metall. Mater. 24 (1990) 79–84, https://doi.org/10.1016/0956-716X(90)90570-7.
[52] S. Suresh, A. Vasudevan, M. Tosten, P. Howell, Microscopic and macroscopic aspects of fracture in lithium-containing aluminum alloys, Acta Metall. 35 (1987) 25–46, https://doi.org/10.1016/0001-6160(87)90210-0.
[53] V. Radmilovic, A. Fox, R. Fisher, G. Thomas, Lithium depletion in precipitate free zones (PFZ's) in Al-Li base alloys, Scripta Metall. 23 (1989) 75–79, https://doi.org/10.1016/0036-9748(89)90096-3.
[54] S. Jha, T. Sanders Jr., M. Dayananda, Grain boundary precipitate free zones in Al-Li alloys, Acta Metall. 35 (1987) 473–482, https://doi.org/10.1016/0001-6160(87)90253-7.
[55] C. Schlesier, E. Nembach, Strengthening of aluminium-lithium alloys by long-range ordered δ'-precipitates, Acta Metall. Mater. 43 (1995) 3983–3990, https://doi.org/10.1016/0956-7151(95)00089-E.